Journal of Membrane Science 711 (2024) 123195

Contents lists available at ScienceDirect

Journal of Membrane Science

journal homepage: www.elsevier.com/locate/memsci

Highly miscible bio-based poly(lactic acid)/acetylated cellulose ether ultrafiltration membranes with improved water permeances

Da-Seul Lim [a,b], Eun-Bi Kim [a,c], Hak-Yong Lee [a], Yong-Nam Kwon [d], Jong-Hak Kim [b], Jae-Chang Lee [a,**], Suwan Myung [a,*]

[a] Research Center for Bio-Based Chemistry, Korea Research Institute of Chemical Technology (KRICT), Ulsan, 44429, Republic of Korea
[b] Department of Chemical and Biomolecular Engineering, Yonsei University, Seoul, 03722, Republic of Korea
[c] Department of Energy Engineering, Hanyang University, Seoul, 04763, Republic of Korea
[d] Department of Urban and Environmental Engineering, Ulsan National Institute of Science and Technology, Ulsan, 44919, Republic of Korea

ARTICLE INFO

Keywords:
Bio-based membrane
Ultrafiltration membrane
Poly(lactic acid)
Acetylated cellulose ether
Blending

ABSTRACT

Biopolymer-based membranes are eco-friendly alternatives to petroleum-based membranes. However, biopolymers often require harsh membrane fabrication conditions due to their low solubilities, which are incompatible with general non-solvent-induced phase separation (NIPS). Thus, establishing mild blending conditions for NIPS membrane production is needed. This study developed ultrafiltration membranes by blending poly (lactic acid) (PLA) and acetylated cellulose ether (ACE), both of which are derived from renewable resources, using NIPS under mild conditions. We investigated the effects of PLA proportion on the structural, chemical, and thermal properties of the blend membranes and assessed polymer miscibility using theoretical models. Results indicated excellent miscibility with a single glass transition temperature. The 1:1 PL A/ACE membrane demonstrated the lowest water contact angle of 45°, 35 % lower than that of the pure PLA membrane. Additionally, its pure water permeance was 179.4 LMH/bar, significantly higher than 103.4 LMH/bar of the pure PLA membrane. Flux recovery ratio at pH = 4 was 69.5 for the blend membrane as compared to 70.6 for the PLA membrane. At pH = 7, all membranes could be fully recovered via physical washing, even those fouled with bovine serum albumin. This study successfully fabricates PLA/ACE-based membranes with outstanding properties under mild conditions.

1. Introduction

Membranes manufactured from biomass-derived polymers have attracted significant attention as alternatives to petroleum-derived polymer membranes [1–5] because CO_2 emissions arising from the excessive use of petrochemicals are continuously increasing, thereby accelerating global warming [6,7]. Most polymeric membranes are manufactured from petrochemicals, for example, polyethersulfone, polysulfone, polyacrylonitrile, PVDF, polyimide, polyamide, and polyvinyl chloride [1], and exhibit significant favorable characteristics such as high thermal and chemical stabilities, mechanical resilience, and cost-effectiveness [8]. Bio-based polymers are promising alternatives to petrochemicals for membrane preparation because of their C-neutral natures and sustainabilities. Thus, developing membranes from biopolymers has garnered extensive research interest [3,9,10].

To date, various bio-based polymers and their derivatives have been developed as membrane materials, and their potentials to replace petroleum-derived polymers have been demonstrated [11,12]. PHB, a bio-based polymer produced via fermentation, has been reported as a promising membrane material [13]. Villegas et al. prepared a PHB pervaporation membrane via EIPS using chloroform as a solvent. In the separation of methanol/MTBE mixtures, the PHB membrane with an acrylic acid layer exhibited high selectivity for methanol and low flux [13]. Moreover, PHBHV-based MF membranes were fabricated by TIPS and NIPS using pore-forming agents. PHBHV membranes prepared using PEG or EG demonstrated larger pore sizes relative to that of a pure PHBHV membrane and a permeate flux of 135 or 480 LMH/bar, respectively [14]. PVP and PEG with different molecular weights and concentrations were incorporated as additives into PHBHV membranes by EIPS using chloroform as the solvent. This study indicated that PVP and PEG affected membrane permeability and pore formation [3].

* Corresponding author.
** Corresponding author.
E-mail addresses: jclee@krict.re.kr (J.-C. Lee), swmyung@krict.re.kr (S. Myung).

https://doi.org/10.1016/j.memsci.2024.123195
Received 29 May 2024; Received in revised form 29 July 2024; Accepted 9 August 2024
Available online 10 August 2024

Nomenclature

(PVDF) Polyvinylidene fluoride
(PHB) Polyhydroxybutyrate
(EIPS) Evaporation-induced phase separation
(MTBE) Methyl *tert*-butyl ether
(PHBHV) Poly(hydroxybutyrate-*co*-hydroxyvalerate)
(MF) Microfiltration
(TIPS) Thermally induced phase separation
(NIPS) Non-solvent-induced phase separation
(PEG) Poly(ethylene glycol)
(EG) Ethylene glycol
(PVP) Polyvinylpyrrolidone
(PBS) Poly(butylene succinate)
(CA) Cellulose acetate
(NMP) 1-Methyl-2-pyrrolidone
(BSA) Bovine serum albumin
(PLA) Poly(lactic acid)
(UF) Ultrafiltration
(PCL) Poly(caprolactone)
(PLLA) Poly(L-lactic acid)
(PDLLA) Poly(D, L-lactic acid)
(PTAT) Poly(tetramethylene adipate-*co*-terephthalate)
(DMF) *N*,*N*-Dimethylformamide
(PEO) Poly(ethylene oxide)
(DI) Deionized
(PBAT) Poly(butylene adipate terephthalate)
(ACE) Acetylated cellulose ether
(VIPS) Vapor-induced phase separation
(PET) Poly(ethylene terephthalate)
(*D*e) Apparent diffusion coefficient
(3D) Three-dimensional
(SEM) Scanning electron microscopy
(AFM) Atomic force microscopy
(WCA) Water contact angle
(FTIR) Fourier-transform infrared
(TGA) Thermogravimetric analysis
(DSC) Differential scanning calorimetry
(PWP) Pure water permeance
(MWCO) Molecular weight cut-off
(FRR) Flux recovery ratio
(2D) Two-dimensional

Furthermore, to enhance the performances of PBS membranes in the purification of raisin wastewater, Ghaffarian et al. prepared PBS/CA membranes with different blend ratios using NMP as the solvent at 50 °C. At an optimum ratio, the membrane exhibited a sponge-like structure, high thermal stability, high permeability owing to hydrophilicity, and high wastewater treatment performance [15].

PLA, economically produced from renewable resources, is one of the most popular biopolymers, and research on the manufacture of PLA-based membranes is being actively conducted. Moriya et al. studied a hollow-fiber-type PLA UF membrane with a permeate flux of ~880 LMH/bar and BSA rejection of 80 % [9]. PCL/PLLA MF membranes were manufactured for cell capturing, and high cell retention was obtained after blending PCL and PLLA in 1,4-dioxane at 90 °C [16]. Despite its advantages as a promising membrane material [17,18], PLA demonstrates the limitations of low glass transition temperature (T_g), brittleness (less than 10 % elongation at break), low toughness, low relative hydrophobicity, and lack of reactive side chains [19,20].

Several methods have been developed to overcome the above-mentioned disadvantages of PLA. Among them, blending PLA with another polymer via a solution process is a simple modification method [21]. Xiong et al. fabricated a PLA/PDLLA stereo-complex membrane with high antifouling performance as compared to that of a pristine PLA membrane. Moreover, the PLA/PDLLA membrane exhibited relatively higher permeability and BSA rejection [10]. Liu et al. employed PTAT to improve the hydrophilicities of PLA membranes and examined their blend miscibilities. They discovered that PLA and PTAT were partially miscible in the blend membrane [22]. Keawsupsak et al. focused on the fabrication of PLA membranes blended with different polymers, such as PBS, PBAT, and PHBV, using NIPS and investigated the filtration performances of these membranes. PLA/PBS exhibited better miscibility than that of PLA/PBAT, and PLA/PHBHV exhibited the best filtration performance [23]. However, the components in the blend membranes were partially miscible even after high-temperature stirring.

Miscibility between polymers is the most important factor in a blending system. In the cases of blend membranes, miscibility is closely related to membrane properties, for example, filtration performance, morphologies, uniformity, and mechanical and thermal properties [24–28]. Immiscibility in blend membranes can cause non-uniform surfaces, defects, and inferior mechanical properties and separation performances due to polymer phase separation [25,27,28]. Therefore, in the cases of blend membranes, considering miscibility is crucial.

PLA, PCL, PHBHV, PBS, and cellulose derivatives have been used to fabricate various types of membranes, and many studies have examined the performances of these biopolymer-based membranes [11]. Nevertheless, in many cases, toxic solvents (e.g., chloroform and dichloromethane) [3,10,14,29] and high dissolution temperatures are required because of the low solubilities of the biopolymers [16,18]. These harsh conditions are not compatible with general NIPS. Therefore, establishing mild blending conditions for NIPS membrane production is urgently required.

Among cellulose derivatives, CA, triacetyl cellulose, ethyl cellulose, carboxymethyl cellulose, and nitrocellulose have been used to fabricate cellulose-derived membranes [12]. ACE is a promising cellulose-derived material for membrane fabrication. Kim et al. prepared an ACE UF membrane using various additives and investigated the membrane fouling performances of these membranes relative to that of a PVDF membrane [30]. According to Han et al. the ACE membrane presented higher mechanical strength while maintaining its hydrophilicity as compared to the cases of the membranes based on CA and cellulose triacetate [31]. Jang et al. constructed a hollow-fiber-type dual-layer ACE membrane by TIPS and NIPS via single-step spinning. Compared to the PVDF membrane, the ACE membrane was more hydrophilic and exhibited better antifouling properties [32]. Jayalakshmi et al. produced CA graft materials (CA-g-(GMA-g-PEG)) and blended or incorporated them with ACE, and the resulting membrane was used to remove metal ions from aqueous solutions. The composite membrane exhibited excellent chlorine stabilization, hydrophilicity, and antifouling properties [33,34]. Additionally, VIPS was employed to fabricate MF membranes with pore sizes of 0.2–0.53 μm, and the molecular weights of the additives were optimized. The resulting membranes exhibited high water permeances and resistances against protein fouling when compared with those of commercial CA membranes [35].

To the best of our knowledge, to date, research on the fabrication of membranes by blending PLA and ACE has not been conducted. Accordingly, in this study, PLA was blended with hydrophilic ACE at mild temperature to achieve PLA/ACE membranes with low hydrophobicities and high T_g values. Miscibility of PLA and ACE was evaluated using several techniques and theoretical models. Then, after preparing the membranes with different blend compositions, their hydrophilicities, filtration performances, and antifouling properties were assessed using BSA as a foulant.

2. Material and methods

2.1. Materials

PLA (2003D) was procured from Natureworks (USA). ACE (Mecellulose®) synthesized on a pilot scale was kindly supplied by Lotte Fine Chemical (Ulsan, South Korea). DMF (>99.8 %, ACS reagent), non-woven PET support (#884, 75 g/m^2, thickness: 0.087 mm, AWA Paper Manufacturing Co. Ltd., Tokushima, Japan), citric acid monohydrate (≥99.0 %, ACS reagent), BSA (≥98 %, heat shock fraction, pH = 7, and molecular weight = 66,000 g/mol), PEG (average molecular weight = 35,000 g/mol), and PEO (average molecular weights = 100,000, 200,000, and 400,000 g/mol) were purchased from Sigma-Aldrich (USA). Anhydrous sodium phosphate monobasic ($NaHPO_4$, 98.0 %) and anhydrous sodium phosphate dibasic (Na_2HPO_4, 99.0 %) were procured from Samchun (Korea). DI water was used in all experiments.

2.2. Characterization of the polymer dope solution

2.2.1. Viscosity and cloud point

Viscosity of each polymer dope solution was measured at 50 rpm using a viscometer (DV-E viscometer, Brookfield Engineering, USA) equipped with an HA-4 spindle (range: 400–80 K). During viscosity measurements, the polymer dope solution was maintained at 50 °C. Average of seven repeated measurements is reported. Cloud point of each polymer solution was visually determined. DI water (100 μL) was injected as a non-solvent into dope solutions with different polymer concentrations (4, 8, 16, and 20 wt%) under stirring at 50 °C. Cloud point was assigned when the polymer solution became turbid and the turbidity persisted for at least 30 min. Thereafter, the proportion of each component (namely, polymer, solvent, and non-solvent) was calculated, and the ternary phase diagram was constructed.

2.2.2. Precipitation kinetics (De of the non-solvent)

De of the non-solvent (DI water) was determined using an optical microscope (ECLIPSE E200, Nikon Instruments, Japan) equipped with a digital camera (IMTcamCCDPro2, IMT Inc., Canada). A drop of the polymer solution was placed between the optical glass and cover glass; then, the non-solvent at 30 °C was dropwise put on the edge of the polymer solution using a micropipette. When the non-solvent contacted the polymer solution, polymer precipitation occurred, and the non-solvent simultaneously diffused into the polymer solution. Diffusion distance of the non-solvent, *d* (cm), was evaluated by the polymer precipitation length and measured every 30 s using i-Solution Lite at a magnification of 4 × . *De* of the non-solvent was calculated using equation (1) [36]:

$$De = \frac{d^2}{4t} \tag{1}$$

where *t* (s) is the time interval.

2.3. Preparation of PLA/ACE membranes

Before all experiments, PLA and ACE were dried overnight at 80 °C in a convection oven. Weights of the polymers were calculated according to the desired polymer ratio, and polymers were dissolved in DMF in a three-necked flask by heating at 50 °C. Compositions of the dope solutions and corresponding sample codes are provided in Table 1. Each dope solution was homogenized to form a clear solution and completely degassed in a convection oven maintained at 50 °C for 4 h.

For membrane preparation, the polymer dope solution was cast to a thickness of 250 μm on the non-woven PET support using a casting knife (Baker, Imoto, Japan). Then, the cast sample was directly immersed in a water bath at 30 °C. Thereafter, the fabricated membranes were stored overnight in flowing water to remove remaining solvent. Finally, all the membranes were stored in a zipper bag with small quantity of DI water followed by refrigeration.

Table 1
Compositions of the PLA/ACE dope solutions.

Membrane	Polymer Ratio (PLA:ACE)	Polymer (wt%)		Solvent (wt%)
		PLA	ACE	DMF
$M_{10:0}$	10:0	16	0	84
$M_{9:1}$	9:1	14.4	1.6	84
$M_{7:3}$	7:3	11.2	4.8	84
$M_{5:5}$	5:5	8	8	84
$M_{3:7}$	3:7	4.8	11.2	84
$M_{1:9}$	1:9	1.6	14.4	84
$M_{0:10}$	0:10	0	16	84

2.4. Membrane characterization

2.4.1. Scanning electron microscopy (SEM) and atomic force microscopy (AFM)

Morphologies of the blend membranes were analyzed by SEM (MIRA3, TESCAN, Czech Republic) at an accelerating voltage of 10 kV. Before analysis, the membranes were coated with Pt for 90 s at 15 mA using a sputter coater (Q150T S, Quorum, UK). To investigate the cross-sectional morphologies, the membranes were frozen and cut under liquid N_2.

Topologies of the membranes were observed using AFM (Dimension Icon, Bruker Co., Germany). Surface roughnesses of the membranes were determined from 3D images with a scan size of 10 × 10 μm^2 in tapping mode.

2.4.2. Water contact angle (WCA) and zeta potential

WCAs of the PLA/ACE membranes were measured using a drop shape analysis system (DSA25 Basic, KRUSS, Germany); the sessile drop method was used to determine the hydrophilicities/hydrophobicities of these membranes. A 5 μL droplet of DI water was placed dropwise on each membrane surface using a microsyringe. Images of the water droplets were acquired every 30 s, and WCAs were evaluated at five randomly chosen locations.

Membrane surface charges were analyzed using a solid surface analyzer (SurPASS™ 3, Anton Paar, Austria) in tangential streaming-potential measurement modes. Automatic titration was performed in the pH range of 3–10 using 0.001 M NaCl (neutral), 0.05 M NaOH (basic), and 0.05 M HCl (acidic) solutions; an adjustable gap cell of 20 mm × 10 mm was put between membrane samples, and a gap of 100 μm was set between the sample surfaces. Zeta potentials were measured by averaging the results of three measurements.

2.4.3. Fourier-transform infrared (FTIR) spectroscopy and Raman spectroscopy

FTIR spectroscopy (Nicolet™ iS50, Thermo Scientific, USA) was conducted to examine the chemical structures of the polymer blends. Spectra were recorded in the wavelength range of 650–4000 cm^{-1} at room temperature with 4 cm^{-1} spectral resolution, and 32 scans were performed to obtain each spectrum.

Raman analysis was conducted using a Raman spectrometer (LabRam Soleil, HORIBA, Japan) equipped with a 50 × ELWD objective (Numerical aperture = 0.6 and Working distance = 11 mm), and the spectrometer grating exhibited 1800 lines/mm (500 nm). Spectra were acquired in the range of 200–4000 cm^{-1} with an acquisition time of 5 s, and a single accumulation was performed for each sample. Raman mapping was conducted at a wavenumber of 872.3 cm^{-1} with an acquisition time of 5 s and two accumulations to clearly distinguish the representative peak of the C-O-C bonds present in the primary chain of PLA. Images were obtained over an area of 20 × 20 μm^2 with a step size of 2 μm, resulting in a total of 400 measurement points in a point-by-

point mode. A 532 nm laser source was utilized, along with a neutral density filter attenuated to 9.4 mW and a hole size of 100 μm. Before analyses, calibration was performed with laser beams emitting at 532 and 785 nm using a Si substrate. LabSpec 6 was employed to operate the mapping system, record the spectra, and process the data.

2.4.4. Thermogravimetric analysis (TGA) and differential scanning calorimetry (DSC)

To investigate the thermal stability of the polymer, TGA was conducted using a thermogravimeter (TG 209 F1 Libra, NETZSCH, Germany) at a N_2 flow rate of 250 mL/min. Approximately 5 mg of each sample was placed in an Al_2O_3 crucible followed by heating from 25 to 100 °C at 10 °C/min rate, maintenance at 100 °C for 1 min, and heating from 100 to 800 °C at 10 °C/min.

DSC (Discovery DSC 2500, TA instrument, USA) was performed at a N_2 gas flow rate of 50 mL/min to examine the miscibility of the polymer blends and their thermal behaviors. The sample was put in an Al pan followed by heating from 40 to 200 °C at a heating rate of 10 °C/min, maintenance at 200 °C for 5 min, and cooling from 200 to 25 °C at 10 °C/min. Finally, these steps were repeated (total two cycles).

T_g was determined as the midpoint between T_{onset} and T_{end} during the second heating cycle [37]. Using the DSC results, the crystallinity of the blend membrane was calculated using equation (2), and the results are presented in Table 2.

$$X_c = \frac{\Delta H_f}{\Delta H_f^{\circ} W} \times 100\ (\%) \tag{2}$$

where X_c is the degree of crystallinity, ΔH_f denotes the apparent enthalpy of fusion obtained from the endothermic melting point area of the DSC curve, ΔH_f° is the enthalpy of fusion of PLA with 100 % crystallinity (93 J/g) [38], and W represents the weight fraction of PLA in the blend.

2.5. Theoretical models for the blend system

Dependence of T_g on the polymer composition can be explained using various theoretical models. Therefore, we compared the theoretical and measured values using the Fox [39], Gordon–Taylor [40], and Kwei equations [41], which are expressed as

$$Fox: \frac{1}{T_{g,b}} = \frac{w_1}{T_{g,1}} + \frac{w_2}{T_{g,2}} \tag{3}$$

$$Gordon - Taylor: T_{g,b} = \frac{w_1 T_{g,1} + k_{GT} w_2 T_{g,2}}{w_1 + k_{GT} w_2} \tag{4}$$

$$Kwei: T_{g,b} = \frac{w_1 T_{g,1} + k_{KW} w_2 T_{g,2}}{w_1 + k_{KW} w_2} + q w_1 w_2 \tag{5}$$

where $T_{g,b}$, $T_{g,1}$, and $T_{g,2}$ are the T_g values (K) of the blend, homogeneous polymer 1, and homogeneous polymer 2, respectively. w_1 and w_2 denote the weight fractions of each polymer component. k_{GT}, k_{Kw}, and q are adjustable parameters that can be fitted using the experimental data. Values were statistically obtained via the best fit of non-linear least squares regression and R-squared values using Python based on the T_g values of seven experiments.

Table 2
DSC results corresponding to the second heating cycle of all PLA/ACE membranes.

	T_g (°C)	T_m (°C)	ΔH_f (J/g)	X_c (%)
$M_{10:0}$	59.4	149.04	16.90	18.06
$M_{9:1}$	59.9	153.52	1.05	1.25
$M_{7:3}$	63.9	N.D.	N.D.	N.D.
$M_{5:5}$	67.7	N.D.	N.D.	N.D.
$M_{3:7}$	102.1	N.D.	N.D.	N.D.
$M_{1:9}$	125.3	N.D.	N.D.	N.D.
$M_{0:10}$	137.7	N.D.	N.D.	N.D.

T_g is the midpoint between T_{onset} and T_{end}, T_m denotes the melting temperature, ΔH_f is the measured enthalpy of fusion, and X_c represents the crystallinity of the system calculated using equation (2). N.D. means not detected.

2.6. Membrane filtration performance

2.6.1. Pure water permeance (PWP)

PWP of each blend membrane was evaluated using a cross-flow filtration system (Fig. 1). All membranes were pre-compacted under 2 bar at room temperature for 2.5 h at a flow rate of 1 L/min to stabilize them. After compaction, PWP of the membrane was measured for 1 h under 1 bar. Permeate samples were acquired at constant time intervals, and PWPs obtained from two measurements were averaged. PWP was calculated as

$$\text{PWP (LMH/bar)} = \frac{V}{(A \times \Delta t \times \Delta P)} \tag{6}$$

where V (L) is the permeate volume, A (m^2) represents the effective membrane area, Δt (h) is the sampling time, and ΔP (bar) denotes the hydraulic pressure applied to the membrane.

2.6.2. Molecular weight cut-off (MWCO)

MWCO was measured to determine the average pore sizes of the membranes. Aqueous solutions of PEG and PEO with different molecular weights (35, 100, 200, and 400 kDa) were separately prepared in DI water at a concentration of 1 g/L. Polymer solutions were filtered in the same way as that specified for calculating PWP; the cross-flow filtration system was operated under 1 bar at a flow rate of 1 L/min. For each membrane, three measurements were conducted. Rejections of PEG and PEO (R) were evaluated using equation (7):

$$\text{R}\ (\%) = \left(1 - \frac{C_p}{C_f}\right) \times 100 \tag{7}$$

where C_f and C_p are the concentrations of PEG and PEO in the feed solution (1 g/L) and permeate, respectively. Calculated R values were plotted against the molecular weight of the polymer, and the molecular weight corresponding to 90 % rejection was determined as MWCO of the membrane.

Based on PEG and PEO, the pore sizes of the membranes were measured using the Stokes–Einstein equation [42]:

For PEO,

$$r_d\ (\text{cm}) = (10.44 \times 10^{-10}) M^{0.587} \tag{8}$$

where r_d (cm) is the Stokes–Einstein radius and M (g/mol) denotes the

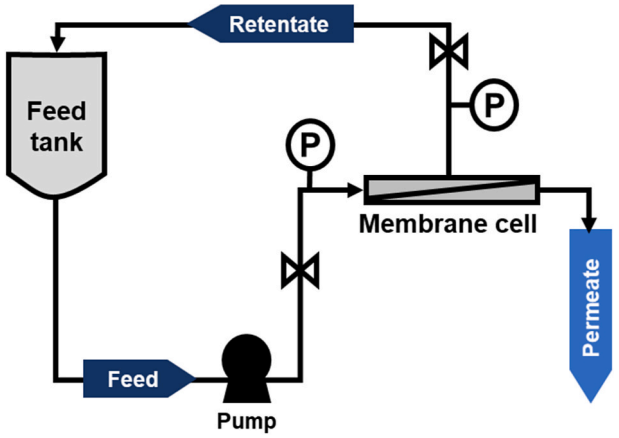

Fig. 1. Schematic of the cross-flow filtration system.

molecular weight of the PEO sample used for determining MWCO.

2.6.3. Antifouling performance and permeance recovery

Antifouling performance was measured as follows: (1) membranes were compacted using a buffer solution (10 mM citrate-phosphate and sodium-phosphate with pH values of 4 and 7, respectively) under 2 bar at a flow rate of 1 L/min for 2.5 h (2) After membrane stabilization, the permeance of the buffer solution was evaluated under 1 bar for 1 h at a flow rate of 1 L/min, and permeate samples were collected at constant time intervals. (3) Then, permeance of a 1 g/L BSA solution (in citrate-phosphate or sodium-phosphate buffer) was measured. (4) After filtration, the BSA-fouled membranes were washed with the buffer solution, and permeance of the buffer was calculated again.

During step (3), BSA concentrations in the feed and permeate were determined in triplicate by Bradford assay [43], and the permeate samples were obtained after BSA filtration for 30 min. Absorbance peak at 595 nm was monitored using a microplate spectrometer (Benchmark Plus Microplate, Bio-Rad, USA). BSA rejection was calculated using equation (7), where C_f and C_p are the concentrations of BSA in the feed and permeate, respectively.

To quantify the antifouling characteristics of the membranes, FRR and flux decline ratio (R_{fd}) were evaluated as follows [44,45]:

$$\mathrm{FRR}(\%) = \frac{F_{Buffer,2}}{F_{Buffer,1}} \times 100 \tag{9}$$

$$R_{fd}(\%) = \left(\frac{F_{Buffer,1} - F_{BSA}}{F_{Buffer,1}}\right) \times 100 \tag{10}$$

where $F_{Buffer,1}$ and $F_{Buffer,2}$ represent the fluxes of the first and second buffer solutions, respectively, and F_{BSA} is the flux of the BSA solution.

2.7. Acid and base stability tests of the membranes

The stabilities of the bio-based membranes was examined using 10 mM HCl (pH = 2) and 10 mM NaOH (pH = 12) aqueous solutions. The concentration of acid and base aqueous solution was performed according to those used for the bio-based membranes reported in the literature [35]. Membranes were cut to obtain with the same weight; then, these membranes were separately stored in each solution for three days at 20 °C, and the stabilities of the membranes were analyzed via TGA after washing with DI water.

3. Results and discussion

3.1. Characterizations of the polymer blend dope solutions

3.1.1. Ternary phase diagrams and diffusion kinetics of the dope solutions

Fig. 2(a) shows the cloud points of the PLA/ACE solutions in DMF, representing their thermodynamic behaviors. Blending PLA with ACE shifted the cloud point to the polymer–solvent axis, indicating less stable thermodynamic states of the PLA/ACE solutions. This behavior indicates that only a small amount of non-solvent (i.e., water) can increase the phase separation rate and induce polymer precipitation [46,47]. Quantities of water required to precipitate polymers in PLA/ACE solutions were lower than those in the cases of pristine PLA and ACE solutions. For $M_{9:1}$, $M_{7:3}$, $M_{5:5}$, $M_{3:7}$, and $M_{1:9}$, polymer precipitation was induced using 3.9, 2.9, 3.4, 3.9, and 5.7 wt% water, respectively, and the pristine PLA and ACE solutions required 6 and 22 wt% water, respectively. Compared to the cases of pristine polymer solutions, a small amount of water could separate the polymer from the blend solution, which indicated low thermodynamic stability of the blend solution [48].

As shown in Fig. 2(b), despite the same total polymer concentrations in all the blends (16 wt%), the viscosities of the solutions were

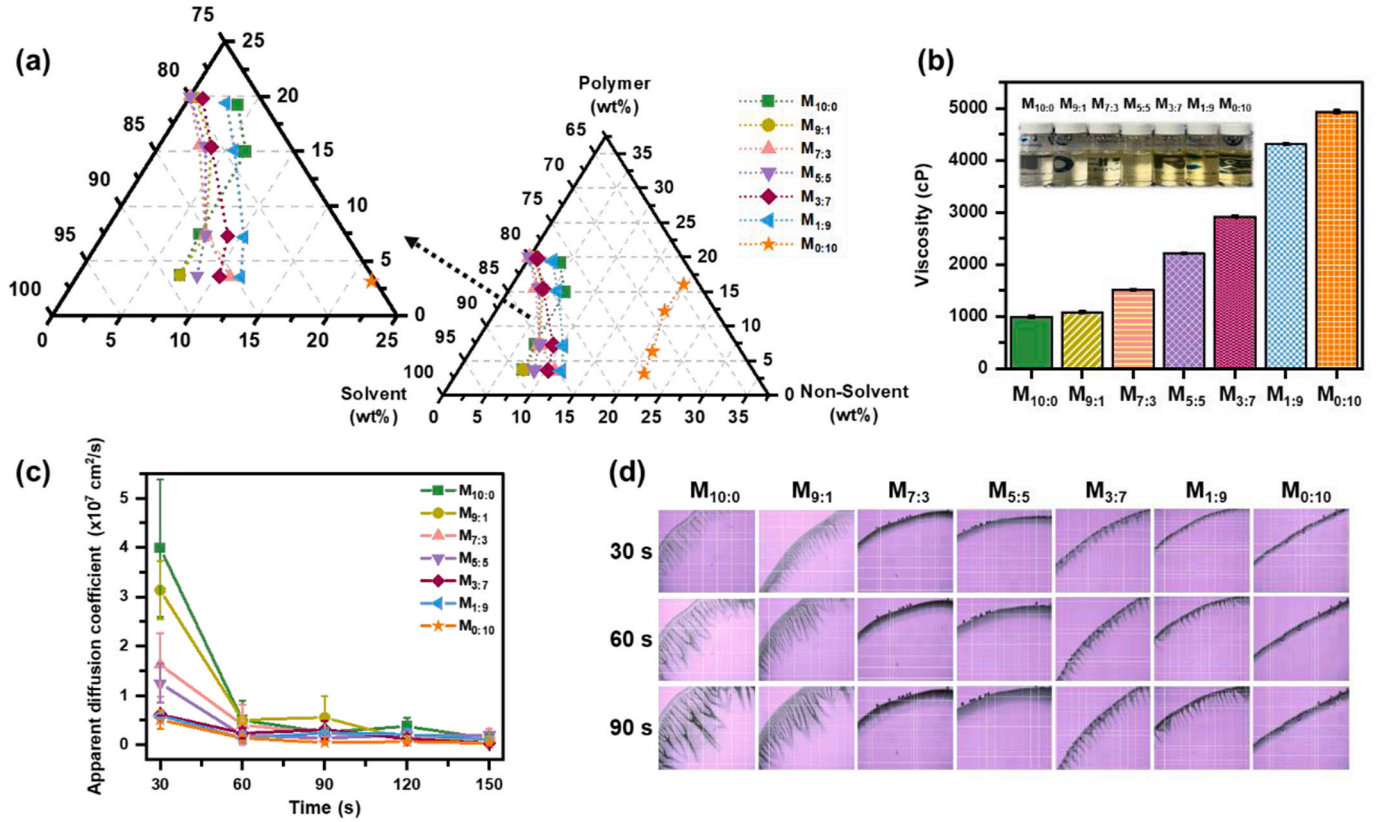

Fig. 2. Characterizations of polymer blend solutions: (a) ternary phase diagram of the polymer blend solution system; (b) viscosities and appearances of the blend solutions; (c) apparent diffusion coefficient of the non-solvent in polymer blend solutions; and (d) optical images obtained at 30, 60, and 90 s.

significantly different. This can affect the variation in *De* of the non-solvent, as depicted in Fig. 2(c) and (d). Fig. 2(c) shows the time-dependent non-solvent diffusion rates for the polymer solutions with different compositions, and Fig. 2(d) depicts the optical images obtained during non-solvent diffusion at constant time intervals. During the initial 30 s, *De* of the non-solvent was the highest for $M_{10:0}$ and gradually decreased with an increase in the viscosities of the dope solutions (Fig. 2 (c)).

Factors influencing the non-solvent diffusion rate were solvent-non-solvent affinity and polymer solution viscosity [49]. In the PLA/ACE solutions, the solvent used demonstrated high affinity to the non-solvent [50]; thus, the dominant factor for the non-solvent diffusion rate was considered to be viscosity (Fig. 2(c)), and the non-solvent diffusion rate decreased with an increase in the viscosity, confirming that the differences between viscosities mainly affect the non-solvent diffusion rate. Nevertheless, over time, the diffusion rate decreased for all the blend solutions because of polymer precipitation [46]. As the viscosity of the dope solution determines the non-solvent diffusion rate [46], it can also impact membrane formation [51]. Relatively fast non-solvent diffusions in $M_{10:0}$ and $M_{9:1}$ contributed to the production of a finger-like pore structure. In contrast, $M_{7:3}$–$M_{0:10}$, which exhibited higher viscosities, formed sponge-like structural matrices due to delayed demixing [46]. However, despite the low non-solvent diffusion rates in the blend solutions, macrovoid growth was observed for $M_{3:7}$ and $M_{1:9}$. $M_{0:10}$ demonstrated the slowest diffusion of the non-solvent, and a sponge-like structure was generated owing to the highest viscosity of the corresponding polymer solution.

3.2. Membrane characterization

3.2.1. Morphologies of the blend membranes

Cross-sectional morphologies of the blend membranes depend on the compositions of these membranes and are also related to the complex interaction between the thermodynamic and kinetic characteristics of the polymer solution and non-solvent [52]. As shown in Fig. 3, the pristine PLA membrane, $M_{10:0}$, exhibited a finger-like structure; however, after the addition of ACE, the membrane morphology changed to a sponge-like structure because of delayed demixing. $M_{7:3}$ and $M_{5:5}$ exhibited a fully sponge-like cross-sections. Although the membranes with other compositions exhibited sponge-like matrices, wide macrovoids were observed for $M_{3:7}$, $M_{1:9}$, and $M_{0:10}$. Macrovoid formation can be caused by numerous factors including surface tension gradient, concentration gradient, and diffusion of solvent from the polymer solution [53].

3.2.2. Structural and thermal properties

Fig. 4 depicts the FTIR spectra and Raman mapping images of the PLA/ACE membranes. Characteristic peaks of $M_{10:0}$ at 1087 and 1182 cm^{-1} in Fig. 4(a) are assigned to the symmetric and asymmetric stretching vibrations of the C-O-C bond, respectively [54,55]. Intensities of these absorption peaks weakened or these peaks disappeared after ACE was blended with PLA. In the FTIR spectrum of $M_{0:10}$, the peaks at 1054 and 1234 cm^{-1} correspond to the stretching vibrations of C-O and C-O-C bonds in ACE [35,56]. C-O and C-O-C peak intensities decreased after the blending of ACE with PLA. Furthermore, the peaks at 2946 and 2999 cm^{-1} are attributed to the symmetric and asymmetric vibrations of C-H in the $–CH_3$ group, respectively [57,58]. Compared with those of the pristine polymer membrane, the characteristic FTIR peaks of the blend membranes are unclearly divided or merged due to changes in the physical state, intra- and inter-H bondings, and ring strains [59]. Overall FTIR and Raman spectra and spectral assignments of the other peaks that are not specifically mentioned are shown in Fig. S3 and Table S1.

Raman spectral mapping can effectively indicate the phase morphologies and compatibilities of the blended polymers [60]. For the Raman mapping of the blend membranes, the peak at 872.3 cm^{-1} corresponding to the C-O-C stretching vibrations of the COO^- bond in the PLA amorphous phase was employed [57,58,61,62]. Fig. 4(b) depicts the Raman mapping images of the blend membranes based on the peak at 872.3 cm^{-1}. In the images, the dark regions represent PLA-rich phases, whereas the bright regions denote ACE-rich phases. With an increase in the ACE proportion, the number of PLA-rich domains decreased, and each phase was evenly distributed in the other phase, indicating that PLA and ACE were appropriately blended in the membrane. Fig. S4 shows the 2D Raman mapping images obtained at 1372.2 cm^{-1}, and the

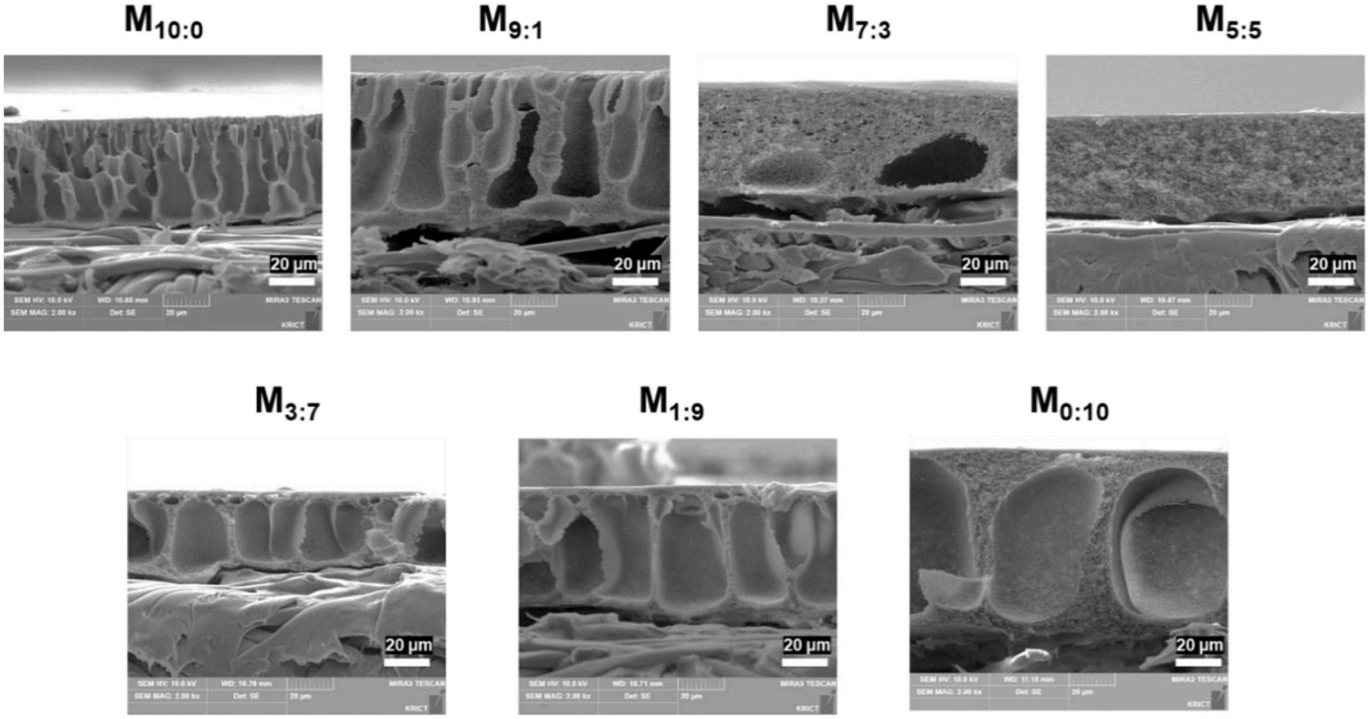

Fig. 3. Cross-sectional SEM images of the PLA/ACE membranes (magnification: 2000 ×).

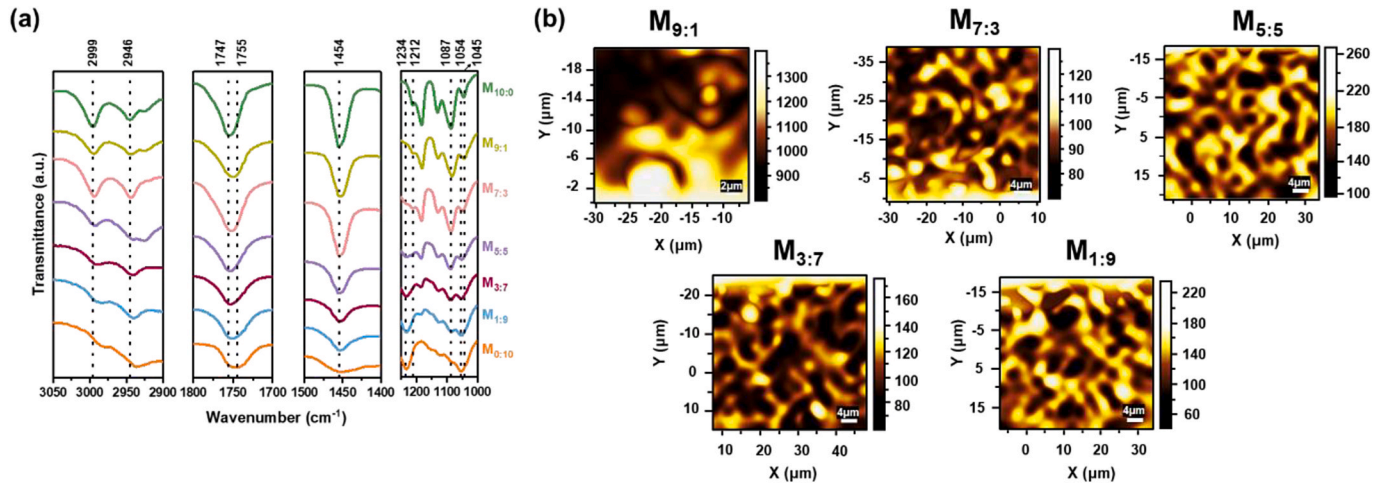

Fig. 4. FTIR spectra and Raman mapping images of the PLA/ACE membranes. (a) FTIR spectra in the range of 1000–3050 cm^{-1} and specific peaks. (b) Raman 2D mapping images of the blend membranes (from $M_{9:1}$ to $M_{1:9}$) at 872.3 cm^{-1}; dark regions represent PLA-rich domains, whereas bright regions denote ACE-rich domains.

cellulose ring structure peak is noticed in the ACE spectrum [63].

By analyzing the second cycle of DSC, the inherent thermal properties of a material can be determined without the influence of thermal history [64]. Curve of $M_{10:0}$ only demonstrated the T_c and T_m peaks of PLA (Fig. 5), suggesting that PLA was semi-crystalline. In sharp contrast, the curve of $M_{0:10}$ exhibited no T_c or T_m peaks and only demonstrated the T_g peak, confirming that ACE was an amorphous polymer as the influence of the long side chains present in the cellulose backbone. In the cases of blend membranes ($M_{9:1}$–$M_{1:9}$), which contained both PLA and ACE, intensities of the T_c and T_m peaks decreased or these peaks disappeared. Moreover, the enthalpy of fusion (ΔH_f) was substantially low for $M_{9:1}$ when compared with that for $M_{10:0}$. This was possibly because the amorphous domain ACE suppressed the crystalline domain PLA [38,65,66]. This effect was confirmed by calculating X_c values of the blend membranes using equation (2), and the results are provided in Table 2. Although ACE was blended at a low ratio, X_c of $M_{9:1}$ was low (1 %). With an increase in the ACE proportion, X_c of the blend membrane decreased to the extent such that the T_m peak did not appear in the DSC curve. This situation is typical for miscible blends composed of an amorphous polymer with high T_g and a crystalline polymer with lower T_g [38]. T_g values of the blends were between those of $M_{10:0}$ and $M_{0:10}$. When more ACE was blended with PLA, T_g increased because ACE exhibited more polymer chain entanglement, thereby enhancing the thermal stability of the blend system. In the second cooling step of DSC (Fig. S6), the cold crystallization temperature T_{cc} peak did not appear in the curves of any of the blend membranes, which was also owing to the impact of ACE [66].

3.2.3. Miscibility of the blend membrane components

3.2.3.1. Theoretical models for the miscibility of polymers in the blend membranes. When the components in a blend polymer are not miscible with each other, the polymer solution becomes turbid, and the T_g peaks of each polymer appear in the thermal analysis curves [60]. Fig. S1 depicts the images of polymer blend solutions of PLA and cellulose-derived polymers, where PLA and ACE solutions at all ratios are transparent and homogeneous at 50 °C. Therefore, from the optical perspective, ACE has higher miscibility with PLA than with other cellulose-derived polymers. Additionally, T_g behaviors of the blend compositions determined via DSC verified polymer miscibility [38,65,67].

Fig. 6 shows T_g of each polymer blend depending on the blend compositions. Compared with the cases of the Fox and Gordon–Taylor equations, a parameter related to the specific interactions of hydrogen bonding (q) was introduced into the Kwei equation to consider the

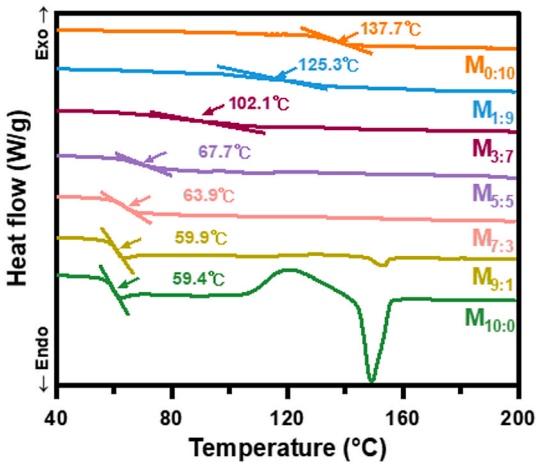

Fig. 5. Second heating curves and T_g values acquired via DSC.

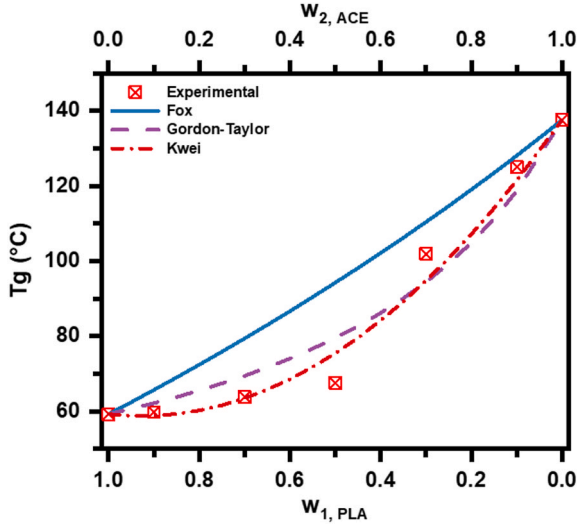

Fig. 6. Analysis of T_g versus weight fraction of each polymer using the Fox, Gordon–Taylor, and Kwei models.

intermolecular interactions in a non-ideal (real) blend system (Table 3) [68]. In the Gordon–Taylor equation, k_{GT} related to the strength of the interaction is 0.35, lower than 1, which indicates that PLA and ACE exhibit weak interactions. Furthermore, the negative deviation of experimental T_g relative to the theoretical curve shows that although these polymers are miscible, they demonstrate a weak interaction [38]. After incorporating an additional fitting parameter (q) into the Kwei equation, the T_g data appropriately fitted with the Kwei model. Q derived from the Kwei equation exhibited a negative value, suggesting weak inter-hydrogen bonding interactions between PLA and ACE. Thus, miscibility cannot be derived from inter-hydrogen bonding. Polymer miscibility is determined by multiple interactions [69]. Besides hydrogen bonding, secondary interactions, such as ion-dipole, electron donor-acceptor, and dipole-dipole interactions, can affect miscibility [59,69]. Herein, a weak interaction between two polymers was discovered via peak variations in the FTIR spectra; however, the factors that lead to the high miscibility of the two polymers require further analysis and research.

3.2.4. Surface properties of the blend membranes

To determine the effect of blending ACE on the hydrophobicities of PLA membranes, WCAs of PLA/ACE membranes were measured at constant time intervals, and the corresponding images are depicted in Fig. S7. WCA of $M_{10:0}$ was approximately 70.8° at 30 s (Fig. 7), implying its relatively hydrophobic nature [70,71]. WCAs of the blend membranes consisting of ACE and PLA in different ratios were low. WCA of $M_{9:1}$ was approximately 20 % lower than that of $M_{10:0}$, whereas those of $M_{7:3}$ and $M_{5:5}$ were approximately 26 and 35 % lower than that of $M_{10:0}$, respectively. However, WCA of $M_{3:7}$ was similar to that of $M_{9:1}$, which was 21 % lower than that of $M_{10:0}$. $M_{1:9}$ and $M_{0:10}$ showed similar WCAs, which were higher than that of $M_{5:5}$. This could be related to the small pore sizes of these membranes, as suggested by the data presented in Table 4, because pore size is a dominant factor affecting WCAs [72]. WCA of $M_{0:10}$ did not significantly decrease over time, which was attributed to the small pore size and dense surface of this membrane, as indicated by its lowest surface roughness of 4.84 nm [73].

$M_{10:0}$ exhibited the highest root-mean-square roughness (R_q) of 15.5 nm; in contrast, the roughnesses of the blend membranes were lower than that of $M_{10:0}$, as can be observed in the case of $M_{5:5}$ (Fig. 8). With an increase in the ACE proportion, the smoothnesses of the blend membrane surfaces increased (Fig. S9). Both WCAs and roughness results revealed that the low WCAs of the blend membranes were not due to low roughness. This is because a surface roughness of 50 nm or less does not affect the contact angle [74]. Overall low WCAs of the blend membrane can be ascribed to the influence of ACE, a hydrophilic polymer. Moreover, the trend demonstrated by the static WCA results can be noticed in the dynamic contact angle results shown in Fig. S8.

Zeta potential is one of the surface characteristics that can impact membrane fouling performance [74,75]. All membranes predominantly exhibit negatively charged surfaces in the pH range of 3–10 (Fig. 9). This can cause electrostatic interactions of the membranes with the solutes in feed depending on the pH conditions. Zeta potential of $M_{10:0}$ is lower than that reported in the literature [76], which appears to be influenced by the zeta potential measurement conditions [77]. Additionally, with an increase in pH, the surface charge became extensively negative, indicating an increase in the repulsion between BSA molecules. In contrast, in the cases of $M_{5:5}$ and $M_{0:10}$, the decreasing trend of zeta potential was not considerable, and the surface charge appeared to induce relatively weaker repulsion or attraction than that in the case of $M_{10:0}$.

Table 3
Parameters, *k* and *q*, and R^2 values for the Fox, Gordon–Taylor, and Kwei models.

Model	k_{GT} or k_{Kw}	*q*	R^2
Fox	–	–	0.8030
Gordon–Taylor	0.35	–	0.9466
Kwei	1.00	−91.59	0.9790

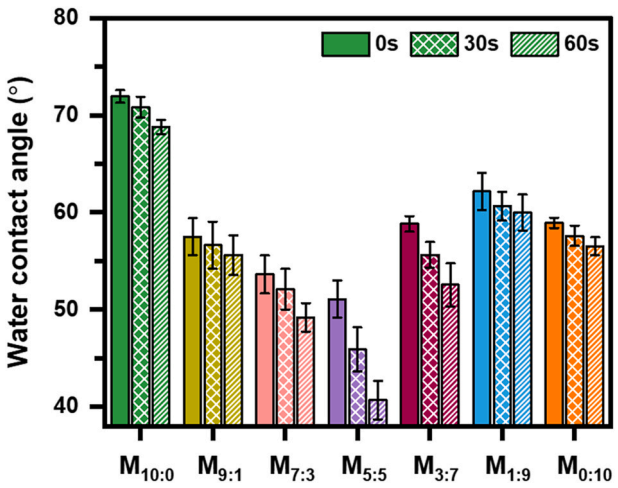

Fig. 7. Water contact angles of the PLA/ACE membranes at 0, 30, and 60 s.

Table 4
Molecular weight cut-off (MWCO) and pore size results of the PLA/ACE membranes.

	MWCO (kDa)	Pore size (nm)
$M_{10:0}$	181 ± 0.4	12.8 ± 0.0
$M_{9:1}$	200 ± 4.3	13.5 ± 0.2
$M_{7:3}$	166 ± 9.1	12.1 ± 0.4
$M_{5:5}$	180 ± 0.5	12.7 ± 0.0
$M_{3:7}$	140 ± 7.0	11.0 ± 0.3
$M_{1:9}$	119 ± 16.9	10.0 ± 0.8
$M_{0:10}$	101 ± 2.0	9.0 ± 0.1

3.3. Membrane performance

3.3.1. PWPs of the membranes

PWPs of the blend membranes were measured after compaction, and the results are depicted in Fig. 10(a). All blend membranes had higher water permeances than that of the pure PLA membrane possibly because ACE increased the hydrophilicity of PLA. PWP increased with an increase in the ACE content up to $M_{3:7}$; $M_{3:7}$ exhibited the highest PWP, which was attributed to the several factors, including morphology, thickness, pore size distribution, and number of pores, affecting PWP [78–81]. $M_{3:7}$–$M_{0:10}$, which demonstrated high viscosities, exhibited relatively high PWPs, which were ascribed to the increases in the number of pores due to delayed phase separation caused by high viscosities of these membranes [82]; contrarily, $M_{1:9}$ and $M_{0:10}$ demonstrated low PWPs because the high viscosities of dope solutions induced small pores and increased membrane thickness during membrane formation [83,84]; moreover, these properties impacted the membrane permeance [78,79].

Fig. 10(b) shows the MWCO profiles of the membranes, which reveal that MWCO rapidly increases with an increase in the ACE content, indicating that the pore size of the membrane gradually decreases with an increase in the ACE content. Although the membrane pore sizes calculated using equation (8) were not significantly different, they were slightly small. These results imply that mixing ACE and PLA can lead to high-performance membranes without considerably changing the pore sizes.

3.3.2. Membrane fouling properties

Antifouling behaviors of the PLA/ACE membranes before and after

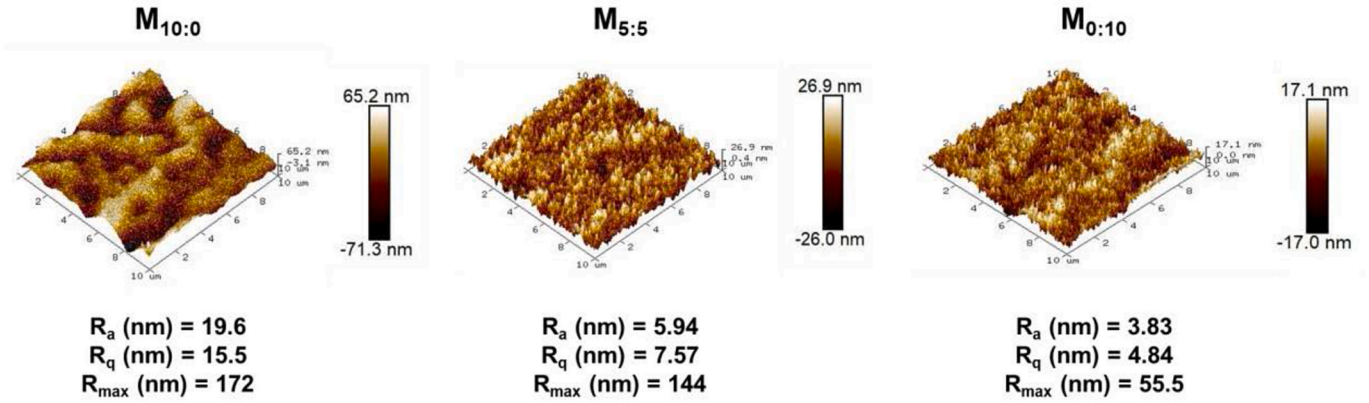

Fig. 8. 3D AFM images of $M_{10:0}$, $M_{5:5}$, and $M_{0:10}$. Abbreviations: R_a, average roughness (nm); R_q, root-mean-square roughness (nm); and R_{max}, maximum peak-to-valley height (nm).

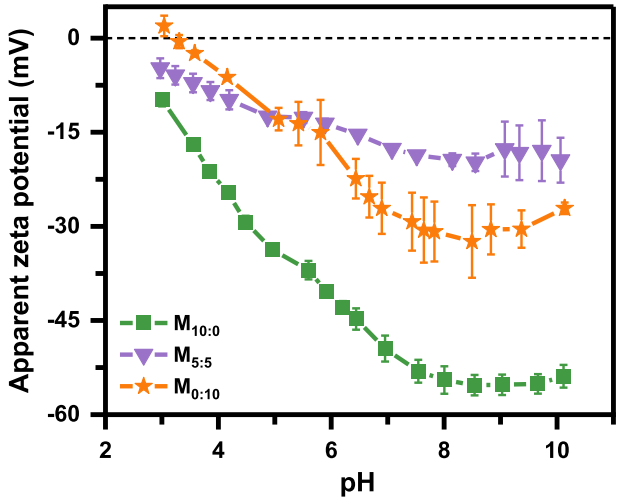

Fig. 9. Apparent zeta potentials of the blend membranes.

fouling with 1 g/L BSA at pH values of 4 and 7 based on the isoelectric point of BSA (pI = 4.8) were compared using buffer solutions. Entire permeance and recovery profiles are depicted in Fig. 11. At pH = 4.0, the permeances of BSA for all membranes sharply decreased by 62–48 % as compared to those of the buffer solutions owing to the adsorption of BSA on the membrane surface via electrostatic attraction [10]. BSA is positively charged at pH = 4 [45], and all the membranes exhibit negative surface charges (Fig. 9). Considering its strongest negative surface charge, $M_{10:0}$ was expected to demonstrate the largest permeance decline; however, $M_{5:5}$ and $M_{0:10}$ with weaker negative surface charges exhibited relatively larger permeance reductions. The reason could be related to pore clogging in the penetrating channels in the membrane [85,86]. If the membrane pore size is larger than the foulant size, the foulant can move into the pores, gradually reducing the effective pore size via adsorption or blockage of the pores, even for $M_{5:5}$ and $M_{0:10}$ with more hydrophilic and smooth surfaces. MWCOs of all membranes are higher than the molecular weight of BSA (66 kDa) (Table 4). Therefore, BSA with size smaller than the pore sizes of the membranes is adsorbed and deposits on the pore wall, thereby narrowing the pore channel for water flow [86,87]. When BSA penetrates the pores, severe fouling is speculated to occur in the membrane pore walls. Results also indicated that the BSA rejection was 100 % at pH = 4 for all membranes. Additionally, during BSA permeation, the permeances of $M_{5:5}$ and $M_{0:10}$ gradually decreased, whereas that of $M_{10:0}$ remained constant, resulting in more pore blockage (Fig. 11(a)) [88].

Nevertheless, during second buffer permeation, the permeance and FRR of $M_{5:5}$ were 96.8 LMH/bar and 69.5 %, respectively, which were similar to those of $M_{10:0}$ (62.6 LMH/bar and 70.6 %, respectively). In contrast, the permeance and FRR of $M_{0:10}$ were 94.6 LMH/bar and 59.0 %, respectively, suggesting that the effect of pore blockage on the performance of $M_{0:10}$ was higher than that on the performance of $M_{5:5}$. Despite the highest R_{fd} (%) of $M_{5:5}$, permeance of $M_{5:5}$ was overall higher than that of $M_{10:0}$.

At pH = 7.0, BSA was negatively charged and the permeance

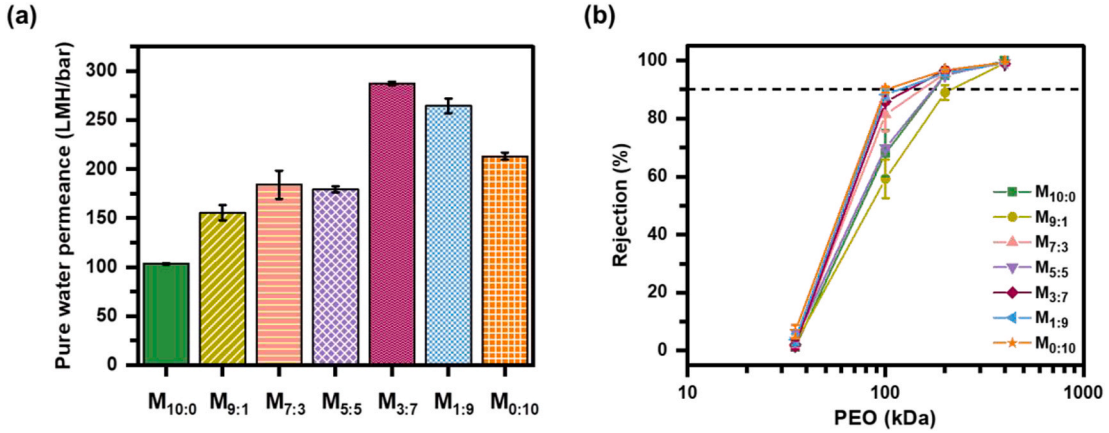

Fig. 10. Membrane filtration performance: (a) pure water permeances (PWPs) of the blend membranes after compaction, as measured at 60 min under 1 bar, and (b) molecular weight cut-offs of the membranes.

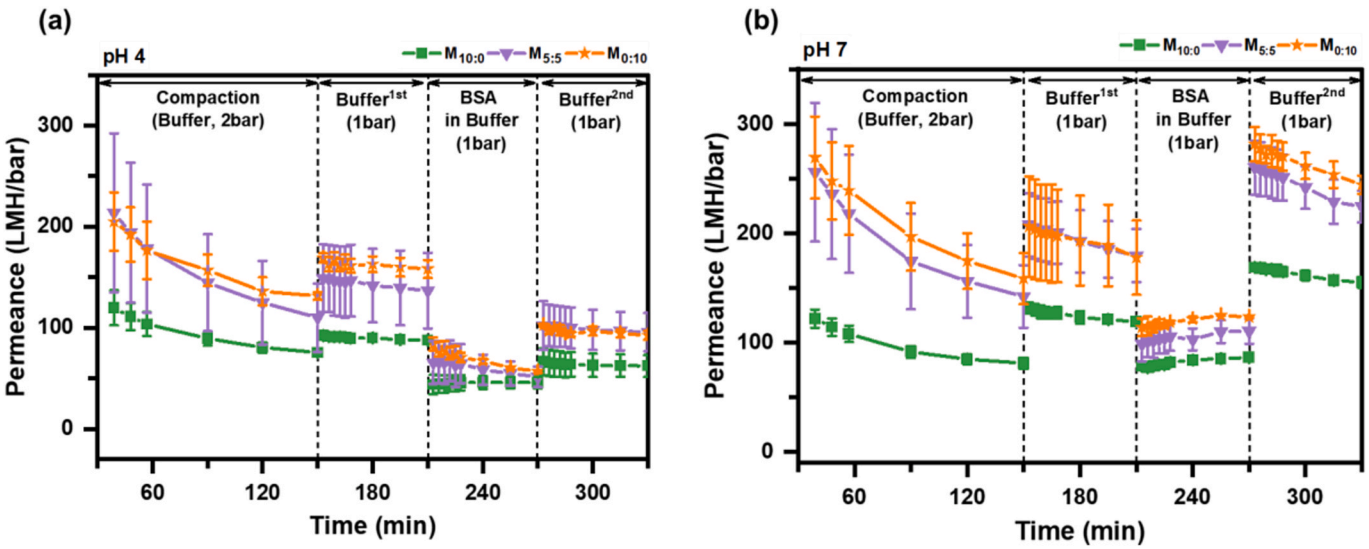

Fig. 11. Fouling permeance profiles of $M_{10:0}$, $M_{5:5}$, and $M_{0:10}$: (a) pH = 4.0 and (b) pH = 7.0.

reduction was lower than that at pH = 4.0 because of a negative repulsive electrostatic interaction between BSA and the membrane [89]. According to Fig. 9, $M_{10:0}$ demonstrated the strongest negative charge at pH = 7, followed by $M_{0:10}$ and $M_{5:5}$. Consequently, the electrostatic repulsive force between BSA and membrane surface was highest in the case of $M_{10:0}$, leading to the lowest R_{fd} (29.6 %); in contrast, R_{fd} of $M_{0:10}$ was 34.0, whereas that of $M_{5:5}$ was 42.0 %. Various factors, for instance, hydrophilicity, surface characteristics, porosity, and pore size, can affect membrane fouling by BSA [90]. Based on the abovementioned results, surface charge plays a more dominant role than hydrophilicity and surface roughness. During BSA permeation, although $M_{5:5}$ and $M_{0:10}$ exhibit higher R_{fd} (%) values than that of $M_{10:0}$, their permeances are higher (107.8 and 123.2 LMH/bar, respectively) than that of $M_{10:0}$ (85.2 LMH/bar). BSA rejection at 30 min was lowest for $M_{10:0}$ (81.0 %), whereas those for $M_{5:5}$ and $M_{0:10}$, which demonstrated smaller pore sizes, were 86.0 and 86.8 %, respectively. Lower adsorption of BSA on the negatively charged membranes at pH = 7 as compared to that at pH = 4.0 was attributed to electrostatic repulsive force between BSA and the membranes.

After the completion of BSA permeation, the BSA molecules adsorbed on the membrane surface were washed with a buffer solution, which loosened the membrane compaction [91]. Therefore, all membranes exhibited slightly higher permeances (157.8, 231.7, and 253.2 LMH/bar for $M_{10:0}$ to $M_{0:10}$) than those during the first buffer permeation (121.0, 185.8, and 186.6 LMH/bar for $M_{10:0}$ to $M_{0:10}$).

Table 5 provides a comparison of the filtration performances of the PLA/ACE membranes fabricated in this study with those of previously reported PLA membranes, indicating that our study successfully prepared UF membranes with high permeations under relatively mild conditions.

3.4. Acid and base stabilities of the membranes

The stability experiments of the membranes were conducted after immersion for three days under acidic and alkaline conditions (Table S3 and Fig. S10). Visual examination revealed that under acidic condition, $M_{10:0}$ slightly degraded, whereas the other blend membranes did not degrade. Under basic condition, all the membranes weakened and became thinner. Residual weight% at 500 °C (R_{500} (%)) significantly decreased under both conditions, as implied by the deformation of the membranes with respect to pH, which facilitated thermal decomposition. Abovementioned results confirmed that the biopolymer-based membranes exhibited inferior acid and alkaline stabilities. Thus, this issue must be overcome to promote the application of biopolymers in membrane in the future.

4. Conclusion

Herein, we fabricated UF membranes by blending two biopolymers (namely, PLA and ACE) derived from renewable resources via NIPS under relatively mild conditions. PLA and ACE had excellent miscibility in the solvent and a single T_g. The PLA/ACE membrane with a blend ratio of 1:1 was hydrophilic and exhibited the lowest WCA of 45°, which was 35 % lower than that of the pristine PLA membrane. The blend membranes demonstrated different morphologies depending on the polymer ratio, higher hydrophilicities than that of the PLA membrane, and higher water permeances (155–287 LMH/bar), at least 1.5-fold that of the PLA membrane. However, substantial BSA fouling occurred in the blend membranes, which was ascribed to the smaller pore sizes and relatively weak surface charges of these membranes. We believe that our study provides a promising green alternative to petroleum-based

Table 5
Comparison of the performances of several PLA-based blend membranes.

Polymer	Ratio	Blending conditions	Preparation	PWP (LMH/bar)	Pore size (nm)	Foulant	Fouling Performance	Type	Ref.
PLA/PLA-PEG-PLA	17:3	DMSO, 130 °C	Wet spinning	115	Not specified	1 g/L BSA at pH = 7.0	FRR: 81 % Rejection: 97.0 %	UF	[29]
PDLA/PLLA	6:12	NMP, 80 °C	NIPS	3325	120	1 g/L BSA at pH = 7.0	FRR: 100 %, Rejection: 88.0 %	UF	[10]
PLA/PBS, PLA/PBAT, and PLA/PHBV	15:1, 15:2, and 15:4	NMP, 90 °C	NIPS	27.6, 18.7, and 65.2	Not specified	1 g/L BSA at pH = 7.0	Rejection: 16.1, 5.7, and 78.7 %	Not specified	[23]
PLA/ACE	5:5	DMF, 50 °C	NIPS	179.4	12.7	1 g/L BSA at = 7.0	FRR: 100 %, Rejection: 86.0 %	UF	This study

polymers for membrane manufacture. Moreover, not only the replacement of petroleum-based polymers with bio-based polymers, but also the application of eco-friendly solvents must be considered in the fabrication of UF membranes. Many challenges are associated with the application of biopolymer membranes, which need to be overcome. Nevertheless, we believe that our research will contribute to the advancement of biopolymer membrane research as it suggests numerous ways to utilize biopolymers and potentials of biopolymers as membrane materials.

CRediT authorship contribution statement

Da-Seul Lim: Writing – original draft, Visualization, Methodology, Investigation. **Eun-Bi Kim:** Methodology, Investigation. **Hak-Yong Lee:** Methodology, Investigation. **Yong-Nam Kwon:** Conceptualization. **Jong-Hak Kim:** Conceptualization. **Jae-Chang Lee:** Supervision. **Suwan Myung:** Writing – review & editing, Writing – original draft, Supervision.

Declaration of competing interest

The authors declare that they have no known competing financial interests or personal relationships that could have appeared to influence the work reported in this paper.

Data availability

Data will be made available on request.

Acknowledgements

This work was supported by the Korea Research Institute of Chemical Technology (KRICT, South Korea) through its core program (KS2442-10). This work was also supported by the Development of Next-Generation Biorefinery Platform Technologies for Leading Bio-based Chemicals Industry Project (NRF-2022M3J5A1056072) and Development of an Integrated Process to Produce Lignocellulosic Biomass-derived Fermentable Sugars for Next-Generation Biorefinery Project (NRF-2022M3J5A1056173) from the National Research Foundation, supported by the Ministry of Science and ICT (South Korea).

Appendix A. Supplementary data

Supplementary data to this article can be found online at https://doi.org/10.1016/j.memsci.2024.123195.

References

[1] V. Vatanpour, A. Dehqan, S. Paziresh, S. Zinadini, A.A. Zinatizadeh, I. Koyuncu, Polylactic acid in the fabrication of separation membranes: a review, Separ. Purif. Technol. 296 (2022) 121433, https://doi.org/10.1016/j.seppur.2022.121433.
[2] N. More, M. Avhad, S. Utekar, A. More, Polylactic acid (PLA) membrane—significance, synthesis, and applications: a review, Polym. Bull. 80 (2) (2023) 1117–1153, https://doi.org/10.1007/s00289-022-04135-z.
[3] P. Tomietto, P. Loulergue, L. Paugam, J.-L. Audic, Biobased polyhydroxyalkanoate (PHA) membranes: structure/performances relationship, Separ. Purif. Technol. 252 (2020) 117419, https://doi.org/10.1016/j.seppur.2020.117419.
[4] J. Zhao, X. Liu, X. Pu, Z. Shen, W. Xu, J. Yang, Preparation method and application of porous poly(lactic acid) membranes: a review, Polymers 16 (13) (2024) 1846.
[5] S. Zereshki, A. Figoli, S.S. Madaeni, S. Simone, J.C. Jansen, M. Esmailinezhad, E. Drioli, Poly(lactic acid)/poly(vinyl pyrrolidone) blend membranes: effect of membrane composition on pervaporation separation of ethanol/cyclohexane mixture, J. Membr. Sci. 362 (1) (2010) 105–112, https://doi.org/10.1016/j.memsci.2010.06.025.
[6] T.M. Joseph, A.B. Unni, K.S. Joshy, D. Kar Mahapatra, J. Haponiuk, S. Thomas, Emerging bio-based polymers from lab to market: current strategies, Market Dynamics and Research Trends C 9 (1) (2023) 30.
[7] N.-A.A.B. Taib, M.R. Rahman, D. Huda, K.K. Kuok, S. Hamdan, M.K.B. Bakri, M.R. M.B. Julaihi, A. Khan, A review on poly lactic acid (PLA) as a biodegradable polymer, Polym. Bull. 80 (2) (2023) 1179–1213, https://doi.org/10.1007/s00289-022-04160-y.
[8] H. Khalil, H.M. Hegab, L. Nassar, V.S. Wadi, V. Naddeo, A.F. Yousef, F. Banat, S. W. Hasan, Asymmetrical ultrafiltration membranes based on polylactic acid for the removal of organic substances from wastewater, J. Water Proc. Eng. 45 (2022) 102510, https://doi.org/10.1016/j.jwpe.2021.102510.
[9] A. Moriya, T. Maruyama, Y. Ohmukai, T. Sotani, H. Matsuyama, Preparation of poly(lactic acid) hollow fiber membranes via phase separation methods, J. Membr. Sci. 342 (1) (2009) 307–312, https://doi.org/10.1016/j.memsci.2009.07.005.
[10] Z. Xiong, Y. Zhong, H. Lin, F. Liu, T. Li, J. Li, PDLA/PLLA ultrafiltration membrane with excellent permeability, rejection and fouling resistance via stereocomplexation, J. Membr. Sci. 533 (2017) 103–111, https://doi.org/10.1016/j.memsci.2017.03.028.
[11] F. Galiano, K. Briceño, T. Marino, A. Molino, K.V. Christensen, A. Figoli, Advances in biopolymer-based membrane preparation and applications, J. Membr. Sci. 564 (2018) 562–586, https://doi.org/10.1016/j.memsci.2018.07.059.
[12] V. Vatanpour, B. Yavuzturk Gul, B. Zeytuncu, S. Korkut, G. İlyasoğlu, T. Turken, M. Badawi, I. Koyuncu, M.R. Saeb, Polysaccharides in fabrication of membranes: a review, Carbohydrate Polym. 281 (2022) 119041, https://doi.org/10.1016/j.carbpol.2021.119041.
[13] M. Villegas, A.I. Romero, M.L. Parentis, E.F. Castro Vidaurre, J.C. Gottifredi, Acrylic acid plasma polymerized poly(3-hydroxybutyrate) membranes for methanol/MTBE separation by pervaporation, Chem. Eng. Res. Des. 109 (2016) 234–248, https://doi.org/10.1016/j.cherd.2016.01.018.
[14] P. Tomietto, M. Carré, P. Loulergue, L. Paugam, J.-L. Audic, Polyhydroxyalkanoate (PHA) based microfiltration membranes: tailoring the structure by the non-solvent induced phase separation (NIPS) process, Polymer 204 (2020) 122813, https://doi.org/10.1016/j.polymer.2020.122813.
[15] V. Ghaffarian, S.M. Mousavi, M. Bahreini, M. Afifi, Preparation and characterization of biodegradable blend membranes of PBS/CA, J. Polym. Environ. 21 (4) (2013) 1150–1157, https://doi.org/10.1007/s10924-012-0551-1.
[16] T. Tanaka, T. Tsuchiya, H. Takahashi, M. Taniguchi, D.R. Lloyd, Microfiltration membrane of polymer blend of poly(l-lactic acid) and poly(ε-caprolactone), Desalination 193 (1) (2006) 367–374, https://doi.org/10.1016/j.desal.2005.06.068.
[17] H. Minbu, A. Ochiai, T. Kawase, M. Taniguchi, D.R. Lloyd, T. Tanaka, Preparation of poly(L-lactic acid) microfiltration membranes by a nonsolvent-induced phase separation method with the aid of surfactants, J. Membr. Sci. 479 (2015) 85–94, https://doi.org/10.1016/j.memsci.2015.01.021.
[18] T. Tanaka, D.R. Lloyd, Formation of poly(l-lactic acid) microfiltration membranes via thermally induced phase separation, J. Membr. Sci. 238 (1) (2004) 65–73, https://doi.org/10.1016/j.memsci.2004.03.020.
[19] E.H. Baran, H.Y. Erbil, Surface modification of 3D printed PLA objects by fused deposition modeling: a review, Colloids and Interfaces 3 (2) (2019) 43.
[20] F. Hassani, S.M. Mousavi, N. Saghatoleslami, V. Ghaffarian, Polyethersulfone/Poly (D,L-lactide) blend membranes: preparation, characterization, and performance, Chem. Eng. Technol. 37 (6) (2014) 1065–1071, https://doi.org/10.1002/ceat.201300477.
[21] L. Zhang, C. Xiong, X. Deng, Miscibility, crystallization and morphology of poly (β-hydroxybutyrate)/poly(d,l-lactide) blends, Polymer 37 (2) (1996) 235–241, https://doi.org/10.1016/0032-3861(96)81093-7.
[22] T.-Y. Liu, W.-C. Lin, M.-C. Yang, S.-Y. Chen, Miscibility, thermal characterization and crystallization of poly(l-lactide) and poly(tetramethylene adipate-co-terephthalate) blend membranes, Polymer 46 (26) (2005) 12586–12594, https://doi.org/10.1016/j.polymer.2005.10.100.
[23] K. Keawsupsak, A. Jaiyu, J. Pannoi, P. Somwongsa, N. Wanthausk, P. Sueprasita, C. Eamchotchawalit, Poly (lactic acid)/biodegradable polymer blend for the preparation of flat-sheet membrane, Jurnal Teknologi 69 (9) (2014) 99–102.
[24] C.-H. Hu, M. Weber, Y.-H. Huang, J.-Y. Lai, T.-S. Chung, Investigating the impact of the sulfonation degree in sulfonated polyphenylsulfone (sPPSU) on PES/sPPSU polymer blend membranes, J. Membr. Sci. 705 (2024) 122890, https://doi.org/10.1016/j.memsci.2024.122890.
[25] S.F. Lai, P.C. Tan, Polyimide blend metal–organic framework-based mixed matrix membrane for gas separation: a review, Asia Pac. J. Chem. Eng. 19 (1) (2024) e2970, https://doi.org/10.1002/apj.2970.
[26] B. Nayak, P. Tanvidkar, B.V.R. Kuncharam, Preparation, characterization, and CO2 permeation testing of cellulose acetate and polyimide blend membranes, Polym. Eng. Sci. 64 (2) (2024) 788–797, https://doi.org/10.1002/pen.26584.
[27] M. Zeng, Z. Fang, C. Xu, Effect of compatibility on the structure of the microporous membrane prepared by selective dissolution of chitosan/synthetic polymer blend membrane, J. Membr. Sci. 230 (1) (2004) 175–181, https://doi.org/10.1016/j.memsci.2003.11.020.
[28] W.F. Yong, H. Zhang, Recent advances in polymer blend membranes for gas separation and pervaporation, Prog. Mater. Sci. 116 (2021) 100713, https://doi.org/10.1016/j.pmatsci.2020.100713.
[29] P. Shen, A. Moriya, S. Rajabzadeh, T. Maruyama, H. Matsuyama, Improvement of the antifouling properties of poly (lactic acid) hollow fiber membranes with poly (lactic acid)–polyethylene glycol–poly (lactic acid) copolymers, Desalination 325 (2013) 37–39, https://doi.org/10.1016/j.desal.2013.06.012.
[30] I.-C. Kim, Y.-S. Jin, D.-H. Song, S.-H. Ahn, Y.-I. Park, B.-S. Kim, J. Jegal, B.-K. Seo, J.-H. Kim, Y.-N. Kwon, C.-J. Mo, J.-J. Lee, D.-S. Kim, S.-H. Lim, Preparation of ultrafiltration membrane by newly synthesized AMC polymer, Desalination Water Treat. 51 (25–27) (2013) 5196–5203, https://doi.org/10.1080/19443994.2013.768425.
[31] J. Han, Y.H. Cho, H. Kong, S. Han, H.B. Park, Preparation and characterization of novel acetylated cellulose ether (ACE) membranes for desalination applications, J. Membr. Sci. 428 (2013) 533–545, https://doi.org/10.1016/j.memsci.2012.10.043.

[32] H. Jang, D.-H. Song, H.-J. Lee, S.-H. Lim, I.-C. Kim, Y.-N. Kwon, Preparation of dual-layer acetylated methyl cellulose hollow fiber membranes via co-extrusion using thermally induced phase separation and non-solvent induced phase separation methods, J. Appl. Polym. Sci. 132 (43) (2015), https://doi.org/10.1002/app.42715.
[33] A. Jayalakshmi, I.-C. Kim, Y.-N. Kwon, Cellulose acetate graft-(glycidylmethacrylate-g-PEG) for modification of AMC ultrafiltration membranes to mitigate organic fouling, RSC Adv. 5 (60) (2015) 48290–48300.
[34] A. Jayalakshmi, I.-C. Kim, Y.-N. Kwon, Application of AMC UF membranes blended with hydrophilic CA-graft copolymer for rejection of Fe(II)/(III) ions using various ligands, J. Ind. Eng. Chem. 51 (2017) 54–63, https://doi.org/10.1016/j.jiec.2017.02.004.
[35] E.-B. Kim, M.-J. Lee, D. Kim, J.-C. Lee, H.-J. Lee, I.-C. Kim, Y.-N. Kwon, S. Myung, Antifouling microfiltration membrane filter based on acetylated cellulose ether using vapor-induced phase separation, Cellulose 31 (1) (2024) 479–495, https://doi.org/10.1007/s10570-023-05650-6.
[36] H. Strathmann, K. Kock, P. Amar, R.W. Baker, The formation mechanism of asymmetric membranes, Desalination 16 (2) (1975) 179–203, https://doi.org/10.1016/S0011-9164(00)82092-5.
[37] I. Iso, 11357-2-Plastics-Differential Scanning Calorimetry (DSC)-Part 2: Determination of Glass Transition Temperature and Glass Transition Step Height, ISO Copyright Office, Geneva, 2013.
[38] G. Zhang, J. Zhang, S. Wang, D. Shen, Miscibility and phase structure of binary blends of polylactide and poly(methyl methacrylate), J. Polym. Sci. B Polym. Phys. 41 (1) (2003) 23–30, https://doi.org/10.1002/polb.10353.
[39] T.G. Fox, Influence of Diluent and of Copolymer Composition on the Glass Temperature of a Poly-Mer System, 1956.
[40] M. Gordon, J.S. Taylor, Ideal copolymers and the second-order transitions of synthetic rubbers. i. non-crystalline copolymers, J. Appl. Chem. 2 (9) (1952) 493–500, https://doi.org/10.1002/jctb.5010020901.
[41] T.K. Kwei, The effect of hydrogen bonding on the glass transition temperatures of polymer mixtures, J. Polym. Sci., Polym. Lett. Ed. 22 (6) (1984) 307–313, https://doi.org/10.1002/pol.1984.130220603.
[42] S. Singh, K.C. Khulbe, T. Matsuura, P. Ramamurthy, Membrane characterization by solute transport and atomic force microscopy, J. Membr. Sci. 142 (1) (1998) 111–127, https://doi.org/10.1016/S0376-7388(97)00329-3.
[43] M.M. Bradford, A rapid and sensitive method for the quantitation of microgram quantities of protein utilizing the principle of protein-dye binding, Anal. Biochem. 72 (1–2) (1976) 248–254.
[44] J. Zhang, Y. Yang, Z. Sun, D. Zhao, Y. Gao, T. Shen, Y. Li, Z. Xie, Y. Huo, H. Li, Ag@BiOBr/PVDF photocatalytic membrane for remarkable BSA anti-fouling performance and insight of mechanism, J. Membr. Sci. 677 (2023) 121611, https://doi.org/10.1016/j.memsci.2023.121611.
[45] D. Kim, I.-C. Kim, Y.-N. Kwon, S. Myung, Novel bio-based polymer membranes fabricated from isosorbide-incorporated poly(arylene ether)s for water treatment, Eur. Polym. J. 136 (2020) 109931, https://doi.org/10.1016/j.eurpolymj.2020.109931.
[46] N. Riyasudheen, A. Sujith, Formation behavior and performance studies of poly (ethylene-co-vinyl alcohol)/poly(vinyl pyrrolidone) blend membranes prepared by non-solvent induced phase inversion method, Desalination 294 (2012) 17–24, https://doi.org/10.1016/j.desal.2012.03.002.
[47] M. Ajdar, A. Azdarpour, A. Mansourizadeh, B. Honarvar, Improvement of porous polyvinylidene fluoride-co-hexafluropropylene hollow fiber membranes for sweeping gas membrane distillation of ethylene glycol solution, Chin. J. Chem. Eng. 28 (12) (2020) 3002–3010, https://doi.org/10.1016/j.cjche.2020.05.004.
[48] S. Li, Z. Cui, L. Zhang, B. He, J. Li, The effect of sulfonated polysulfone on the compatibility and structure of polyethersulfone-based blend membranes, J. Membr. Sci. 513 (2016) 1–11, https://doi.org/10.1016/j.memsci.2016.04.035.
[49] H.-L. Yang, M.-H. Wu, M.B.M.Y. Ang, C.-L. Li, H.-A. Tsai, K.-R. Lee, Mechanism of membrane formation from mixing cellulose acetate and carbon quantum dots together in different solvents, J. Taiwan Inst. Chem. Eng. 150 (2023) 105082, https://doi.org/10.1016/j.jtice.2023.105082.
[50] L. Yu, F. Yang, M. Xiang, Phase separation in a PSf/DMF/water system: a proposed mechanism for macrovoid formation, RSC Adv. 4 (80) (2014) 42391–42402, https://doi.org/10.1039/C4RA06088A.
[51] Z. Zhang, Q. An, Y. Ji, J. Qian, C. Gao, Effect of zero shear viscosity of the casting solution on the morphology and permeability of polysulfone membrane prepared via the phase-inversion process, Desalination 260 (1) (2010) 43–50, https://doi.org/10.1016/j.desal.2010.05.002.
[52] S. Mazinani, S. Darvishmanesh, A. Ehsanzadeh, B. Van der Bruggen, Phase separation analysis of Extem/solvent/non-solvent systems and relation with membrane morphology, J. Membr. Sci. 526 (2017) 301–314, https://doi.org/10.1016/j.memsci.2016.12.031.
[53] D.-M. Wang, F.-C. Lin, T.-T. Wu, J.-Y. Lai, Formation mechanism of the macrovoids induced by surfactant additives, J. Membr. Sci. 142 (2) (1998) 191–204, https://doi.org/10.1016/S0376-7388(97)00322-0.
[54] K. Yuniarto, Y.A. Purwanto, S. Purwanto, B. Welt, H. Purwadaria, T. Sunarti, Infrared and Raman studies on polylactide acid and polyethylene glycol-400 blend. https://doi.org/10.1063/1.4945555, 2016.
[55] F.G. Orozco, A. Valadez-González, J.A. Domínguez-Maldonado, F. Zuluaga, L. E. Figueroa-Oyosa, L.M. Alzate-Gaviria, Lactic acid yield using different bacterial strains, its purification, and polymerization through ring-opening reactions, International Journal of Polymer Science 2014 (2014) 365310, https://doi.org/10.1155/2014/365310.
[56] S. Cheng, A. Huang, S. Wang, Q. Zhang, Effect of different heat treatment temperatures on the chemical composition and structure of Chinese fir wood, Bioresources 11 (2016) 4006–4016, https://doi.org/10.15376/biores.11.2.4006-4016.
[57] A. Pandele, A. Constantinescu, C. Radu, F. Miculescu, Ş.I. Voicu, L. Ciocan, Synthesis and characterization of PLA-micro-structured hydroxyapatite composite films, Materials 13 (2020), https://doi.org/10.3390/ma13020274.
[58] E.V. Vasconcelos, F.B. da Luz, S.P.A. da Paz, M.A.L. dos Reis, A.C.R. da Silva, M. F. Passos, C.A.G. Barboza, S.N. Monteiro, V.S. Candido, Nanostructured 3D bioprinting of PLA with bioglass-CNT scaffolds for osseus tissue graft manufacturing, J. Mater. Res. Technol. 23 (2023) 5923–5938, https://doi.org/10.1016/j.jmrt.2023.02.171.
[59] N.F. Mazuki, Y. Nagao, M.Z. Kufian, A.S. Samsudin, The influences of PLA into PMMA on crystallinity and thermal properties enhancement-based hybrid polymer in gel properties, Mater. Today: Proc. 49 (2022) 3105–3111, https://doi.org/10.1016/j.matpr.2020.11.037.
[60] J. Parameswaranpillai, S. Thomas, Y. Grohens, 1 Polymer Blends : State of the Art , New Challenges , and Opportunities, 2014.
[61] S. Singh, P. Anthony, A. Chowdhury, High molecular weight poly(lactic acid) synthesized with apposite catalytic combination and longer time, Orient. J. Chem. 34 (2018) 1984–1990, https://doi.org/10.13005/ojc/3404036.
[62] J.E. Oliveira, L.H.C. Mattoso, W.J. Orts, E.S. Medeiros, Structural and morphological characterization of micro and nanofibers produced by electrospinning and solution blow spinning: a comparative study, Adv. Mater. Sci. Eng. 2013 (2013) 409572, https://doi.org/10.1155/2013/409572.
[63] M. Ioniță, L.E. Crică, S.I. Voicu, S. Dinescu, F. Miculescu, M. Costache, H. Iovu, Synergistic effect of carbon nanotubes and graphene for high performance cellulose acetate membranes in biomedical applications, Carbohydrate Polym. 183 (2018) 50–61, https://doi.org/10.1016/j.carbpol.2017.10.095.
[64] C. Miyazaki, I. Medeiros, J. Matos, L. Rodrigues Filho, Thermal characterization of dental composites by TG/DTG and DSC, J. Therm. Anal. Calorim. 102 (1) (2010) 361–367.
[65] A. Mohamed, S.H. Gordon, G. Biresaw, Poly(lactic acid)/polystyrene bioblends characterized by thermogravimetric analysis, differential scanning calorimetry, and photoacoustic infrared spectroscopy, J. Appl. Polym. Sci. 106 (3) (2007) 1689–1696, https://doi.org/10.1002/app.26783.
[66] M. Gonzalez-Garzon, S. Shahbikian, M.A. Huneault, Properties and phase structure of melt-processed PLA/PMMA blends, J. Polym. Res. 25 (2) (2018) 58, https://doi.org/10.1007/s10965-018-1438-1.
[67] J.L. Eguiburu, J.J. Iruin, M.J. Fernandez-Berridi, J. San Román, Blends of amorphous and crystalline polylactides with poly(methyl methacrylate) and poly (methyl acrylate): a miscibility study, Polymer 39 (26) (1998) 6891–6897, https://doi.org/10.1016/S0032-3861(98)00182-7.
[68] N. Zeggai, Z. Bouberka, F. Dubois, T. Bouchaour, B. Dali Youcef, L. Delarace, J. Potier, P. Supiot, U. Maschke, Effect of structure on the glass transition temperatures of linear and crosslinked poly(isobornylacrylate-co-isobutylacrylate), J. Appl. Polym. Sci. 138 (20) (2021) 50449, https://doi.org/10.1002/app.50449.
[69] A.A. Lin, T.K. Kwei, A. Reiser, On the physical meaning of the Kwei equation for the glass transition temperature of polymer blends, Macromolecules 22 (10) (1989) 4112–4119, https://doi.org/10.1021/ma00200a052.
[70] M. Calosi, A. D'Iorio, E. Buratti, R. Cortesi, S. Franco, R. Angelini, M. Bertoldo, Preparation of high-solid PLA waterborne dispersions with PEG-PLA-PEG block copolymer as surfactant and their use as hydrophobic coating on paper, Prog. Org. Coating 193 (2024) 108541, https://doi.org/10.1016/j.porgcoat.2024.108541.
[71] E. Gorgun, A. Ali, M.S. Islam, Biocomposites of poly(lactic acid) and microcrystalline cellulose: influence of the coupling agent on thermomechanical and absorption characteristics, ACS Omega 9 (10) (2024) 11523–11533, https://doi.org/10.1021/acsomega.3c08448.
[72] S.H. Woo, J. Park, B.R. Min, Relationship between permeate flux and surface roughness of membranes with similar water contact angle values, Separ. Purif. Technol. 146 (2015) 187–191, https://doi.org/10.1016/j.seppur.2015.03.048.
[73] D.F. Stamatialis, C.R. Dias, M. Norberta de Pinho, Atomic force microscopy of dense and asymmetric cellulose-based membranes, J. Membr. Sci. 160 (2) (1999) 235–242, https://doi.org/10.1016/S0376-7388(99)00089-7.
[74] M.F. Ismail, M.A. Islam, B. Khorshidi, A. Tehrani-Bagha, M. Sadrzadeh, Surface characterization of thin-film composite membranes using contact angle technique: review of quantification strategies and applications, Adv. Colloid Interface Sci. 299 (2022) 102524, https://doi.org/10.1016/j.cis.2021.102524.
[75] L. Nassar, H.M. Hegab, H. Khalil, V.S. Wadi, V. Naddeo, F. Banat, S.W. Hasan, Development of green polylactic acid asymmetric ultrafiltration membranes for nutrient removal, Sci. Total Environ. 824 (2022) 153869, https://doi.org/10.1016/j.scitotenv.2022.153869.
[76] K. Wojciechowski, E. Klodzinska, Zeta potential study of biodegradable antimicrobial polymers, Colloids Surf. A Physicochem. Eng. Asp. 483 (2015) 204–208, https://doi.org/10.1016/j.colsurfa.2015.04.033.
[77] S. Salgın, U. Salgın, N. Soyer, Streaming potential measurements of polyethersulfone ultrafiltration membranes to determine salt effects on membrane zeta potential, Int. J. Electrochem. Sci. 8 (3) (2013) 4073–4084, https://doi.org/10.1016/S1452-3981(23)14454-3.
[78] F. Cuperus, C. Smolders, Characterization of UF membranes: membrane characteristics and characterization techniques, Adv. Colloid Interface Sci. 34 (1991) 135–173.
[79] K.-J. Hwang, P.-Y. Sz, Effect of membrane pore size on the performance of cross-flow microfiltration of BSA/dextran mixtures, J. Membr. Sci. 378 (1) (2011) 272–279, https://doi.org/10.1016/j.memsci.2011.05.018.
[80] A. Rahimpour, S.S. Madaeni, Polyethersulfone (PES)/cellulose acetate phthalate (CAP) blend ultrafiltration membranes: preparation, morphology, performance and

antifouling properties, J. Membr. Sci. 305 (1) (2007) 299–312, https://doi.org/10.1016/j.memsci.2007.08.030.
[81] H.B. Park, J. Kamcev, L.M. Robeson, M. Elimelech, B.D. Freeman, Maximizing the right stuff: the trade-off between membrane permeability and selectivity, Science 356 (6343) (2017) eaab0530, https://doi.org/10.1126/science.aab0530.
[82] B. Chakrabarty, A.K. Ghoshal, M.K. Purkait, Preparation, characterization and performance studies of polysulfone membranes using PVP as an additive, J. Membr. Sci. 315 (1) (2008) 36–47, https://doi.org/10.1016/j.memsci.2008.02.027.
[83] S. Hamzah, N. Ali, M. Ariffin, A. Ali, A. Mohammad, High performance of polysulfone ultrafiltration membrane: effect of polymer concentration, J. Eng. Appl. Sci. 9 (12) (2014) 2543–2550.
[84] G. Bakeri, A.F. Ismail, M. Shariaty-Niassar, T. Matsuura, Effect of polymer concentration on the structure and performance of polyetherimide hollow fiber membranes, J. Membr. Sci. 363 (1) (2010) 103–111, https://doi.org/10.1016/j.memsci.2010.07.018.
[85] F. Wang, V.V. Tarabara, Pore blocking mechanisms during early stages of membrane fouling by colloids, J. Colloid Interface Sci. 328 (2) (2008) 464–469, https://doi.org/10.1016/j.jcis.2008.09.028.
[86] W. Zhang, L. Ding, Investigation of membrane fouling mechanisms using blocking models in the case of shear-enhanced ultrafiltration, Separ. Purif. Technol. 141 (2015) 160–169, https://doi.org/10.1016/j.seppur.2014.11.041.
[87] H. Yang, X. Yu, J. Liu, Z. Tang, T. Huang, Z. Wang, Q. Zhong, Z. Long, L. Wang, A concise review of theoretical models and numerical simulations of membrane fouling, Water 14 (21) (2022) 3537.
[88] C. Duclos-Orsello, W. Li, C.-C. Ho, A three mechanism model to describe fouling of microfiltration membranes, J. Membr. Sci. 280 (1) (2006) 856–866, https://doi.org/10.1016/j.memsci.2006.03.005.
[89] M. Hashino, K. Hirami, T. Ishigami, Y. Ohmukai, T. Maruyama, N. Kubota, H. Matsuyama, Effect of kinds of membrane materials on membrane fouling with BSA, J. Membr. Sci. 384 (1) (2011) 157–165, https://doi.org/10.1016/j.memsci.2011.09.015.
[90] M.-J. Corbatón-Báguena, S. Álvarez-Blanco, M.-C. Vincent-Vela, Fouling mechanisms of ultrafiltration membranes fouled with whey model solutions, Desalination 360 (2015) 87–96, https://doi.org/10.1016/j.desal.2015.01.019.
[91] L.-F. Fang, B.-K. Zhu, L.-P. Zhu, H. Matsuyama, S. Zhao, Structures and antifouling properties of polyvinyl chloride/poly(methyl methacrylate)-graft-poly(ethylene glycol) blend membranes formed in different coagulation media, J. Membr. Sci. 524 (2017) 235–244, https://doi.org/10.1016/j.memsci.2016.11.026.